Available at
http://pvamu.edu/aam
Appl. Appl. Math.
ISSN: 1932-9466

Applications and Applied Mathematics:
An International Journal
(AAM)

Vol. 12, Issue 1 (June 2017), pp. 305 - 318

Two-dimensional model of nanoparticle deposition in the alveolar ducts of the human lung

Anju Saini, V.K. Katiyar and Pratibha

Department of Mathematics
Indian Institute of Technology
Roorkee-India
anju.iitr@gmail.com; vktmafma20@gmail.com; pratibhag@rediffmail.com

Received August 5, 2016; Accepted December 7, 2016

Abstract

In this paper a mathematical model for nanoparticle deposition in the alveolar ducts of the human lung airways is proposed. There were huge inconsistencies in deposition between ducts of a particular generation and inside every alveolated duct, signifying that limited particle concentrations can be much bigger than the mean acinar concentration. A large number of particles are unsuccessful to way out the structure during expiration. Finite difference method has been used to solve the unsteady nonlinear Navier–Stokes equations in cylindrical coordinate system governing flow assuming axial symmetry under laminar flow condition so that the problem efficiently turns into two-dimensional. An extensive quantitative study is performed through numerical computations of the preferred quantities having physiological importance through their graphical demonstration so as to authenticate the applicability of the current model.

Keywords: Laminar flow; Human Lung; Finite difference method; Nanoparticle deposition

MSC 2010 No.: 92C10; 92B05; 74F10

1. Introduction

The deposition of inhaled particles in human lung is the joint action of biological and physical aspects. The lung morphology and respiratory physiology comprises of the fluid dynamics of the inhaled air and particles. Cheng and Swift (1995), Cheng et al. (1996) and Smith et al. (2001) published their measurements of mass transfer and deposition of nanoparticles (3.6–150 nm) in human nasal, oral and upper tracheobronchial airways; Cohen et al. (1990) described their experimental work on nanoparticle deposition in an upper tracheobronchial airway; Kelly et al. (2004) described the nasal deposition efficiencies of nanoparticles with diameter between 5 and 150 nm; Kim and Jaques (2000 and 2004) reported total respiratory tract deposition fraction of nanoparticles (8–100 nm) in healthy adults. Kim and Jaques (2004) also described regional deposition fractions of nanoparticles (40–100 nm) in tracheobronchial and alveolar regions of healthy adults.

Illustrations of numerical simulations for nanoparticle deposition were given by Hofmann et al. (2003), Saini et al. (2014), Shi et al. (2004), Xi and Longest (2008a), Zhang and Kleinstreuer (2004) and Zhang et al. (2005). These studies alert separately on the nasal or oral and upper tracheobronchial airways (from trachea to generation G6). The performance of aerosols in the lung is still weakly understood, particularly in the alveolar region of the lung. In a variety of conditions, mathematical models are regularly used with experimental studies. Mathematical models not simply assist to understand experimental data but also let forecast to be prepared for cases where experimental data do not exist. In general, experimental and numerical analysis show that the particle size, inhalation flow rate and airway geometric features are main issues manipulating nanoparticle deposition in human lung airways.

Although it is generally established that fine particles (smaller than 2.5 μm) can go deep into the alveolar region of the lung, no procedure for allocating accurate direct in vivo measurements is yet available. Therefore, information on aerosol deposition patterns and mixing procedures has relied on indirect experimental measurements and mostly on models of aerosol transport within the lung. For example, Ingham (1991) and Martonen et al. (1996) derived analytical terms for calculating nanoparticle deposition efficiencies in straight circular pipes with different inlet conditions. Industrial fluid-particle flow procedures are usually steady-state by design; in contrast, any breathing pattern is oscillatory. Most researchers Ingham (1991), Lee and Lee (2002), Martonen et al. (1996) picked the mass transport equation in a variety of forms to simulate ultrafine particle convection and dispersion, with Hofmann et al. (2003) and Moskal and Gradon (2002) being exceptions. Saini et al. (2015 and 2016) discussed the incompressible boundary layer flow of a two-phase particulate suspension which is explored numerically over a tube with axisymmetric constriction. In comparison to the species mass transport approach, a two-fluid model (Kleinstreuer 2003) could be developed where the particle field is explained by a second vector equation and coupled to the carrier fluid flow equation via an interphase drag force. This was a fundamental study which exactly forecasts nanoparticle deposition and a first step in the investigation of the outcome of ultrafine toxic or therapeutic particles in the human lung. We have concentrated on modeling of aerosol transport and deposition in the alveolar zone (Figure 1) of the lung (Severinghaus et al. 1998).

The aim is to build up a model that permits the study of aerosol dynamics in a region of the lung where direct collected works of experimental data is not sufficient. Pulsatile flows are usually generated by a periodically time varying pressure. Nayfeh (1966) has studied the pulsatile flow of a dusty fluid through a single symmetrical constricted channel. He described a new model of a multi-generation structure of alveolated ducts and explained the numerical technique accustomed to calculate both the flow field and the trajectories of 100nm-diameter particles. Sturm (2015) has presented the theoretical deposition of nanoparticles in the alveoli of the HRT, since this lung compartment is most susceptible for nanoparticle-induced insuffiiencies. Besides the influence of inhalation flow also the role of particle geometry and density with regard to alveolar deposition is subjected to a detailed investigation.

The present work is concerned with pulsatile flow of dusty fluid through a pipe consisting of axisymmetric distributed constrictions described by the wall radius *R*. Through an extra drag force caused by dust particles the fluid flow is assumed to be governed by Navier-Stokes equations. Governing equations are solved numerically by using suitable finite difference method. The expressions for the velocities of fluid and dust particles have been obtained.

2. Mathematical model

At every one of the eight outlets of the central part, a parallel configuration was linked so that imitations could be sustained in 6 successive generations (Figure 2) (Darquenne 2001). These configurations are introduced as the peripheral parts. The imitations in every one of the peripheral parts were carried out individually.

The functioning fluid is air, and the calculations are carried out for fix Reynolds number 1201. At this Reynolds number (ranging from 200 to 1600), the flow is typical laminar. For human respiration, the maximum pressure drop is ≈ 35mm H_2O (Smith et al. 2001), and the atmospheric pressure is ≈10357mm H_2O. Since

$$\frac{d\rho}{\rho}=\frac{dP}{P}=\frac{35\,\text{mm}}{10357\,\text{mm}}=0.338\,\%,$$

where ρ is the density and P is the pressure, the density change of air can be negligible, i.e., air is incompressible.

2.1. Governing Equation

The alveolar sac is recognized as a cylindrical elastic tube of the circular cross section having an incompressible non-Newtonian fluid. The motion of dusty viscous incompressible fluid is represented to be laminar, unsteady, two-dimensional, axi-symmetric and fully developed. Under these assumptions, the equations governing the fluid flow containing solid particles may be written in the cylindrical coordinates system (r,z,θ) as

Equation of continuity

$$\frac{\partial u_r}{\partial r}+\frac{u_r}{r}+\frac{\partial u_z}{\partial z}=0, \tag{1}$$

$$\frac{\partial v_r}{\partial r}+\frac{v_r}{r}+\frac{\partial v_z}{\partial z}=0. \tag{2}$$

Equation of axial momentum

$$\frac{\partial u_z}{\partial t}+u_r\frac{\partial u_z}{\partial r}+u_z\frac{\partial u_z}{\partial z}=-\frac{1}{\rho}\frac{\partial p}{\partial z}+\nu\left(\frac{\partial^2 u_z}{\partial r^2}+\frac{1}{r}\frac{\partial u_z}{\partial r}+\frac{\partial^2 u_z}{\partial z^2}\right)+\frac{KN_0}{\rho}(v_z-u_z), \tag{3}$$

$$\frac{\partial v_z}{\partial t}+v_z\frac{\partial v_z}{\partial z}+v_r\frac{\partial v_z}{\partial r}=\frac{K}{m}(u_z-v_z). \tag{4}$$

Equation of radial momentum

$$\frac{\partial u_r}{\partial t}+u_r\frac{\partial u_r}{\partial r}+u_z\frac{\partial u_r}{\partial z}=-\frac{1}{\rho}\frac{\partial p}{\partial r}+\nu\left(\frac{\partial^2 u_r}{\partial r^2}+\frac{1}{r}\frac{\partial u_r}{\partial r}+\frac{\partial^2 u_r}{\partial z^2}-\frac{u_r}{r^2}\right)+\frac{KN_0}{\rho}(v_r-u_r), \tag{5}$$

$$\frac{\partial v_r}{\partial t}+v_z\frac{\partial v_r}{\partial z}+v_r\frac{\partial v_r}{\partial r}=\frac{K}{m}(u_r-v_r). \tag{6}$$

Here, $u_z(r,z,t)$ and $u_r(r,z,t)$ represent the axial and the radial velocity components of the fluid respectively, $v_z(r,z,t)$ and $v_r(r,z,t)$ represents the axial and the radial velocity components of the dust particles respectively, p is the static pressure, ρ is the air density, ν is the kinematic viscosity parameter, N_0 is the number density, m is the mass of the dust particle, K is the Stokes resistance coefficient which, for spherical particles, is $6\pi\mu r_p$, μ being the coefficient of viscosity of the fluid and r_p the radius of the particles. Since the lumen radius R is sufficiently small, (5) - (6) simply reduce to $\frac{\partial p}{\partial r}=0$ and thus can be omitted. The pressure gradient ${\partial p}/{\partial z}$ appearing in (3), is given by

$$-\frac{\partial p}{\partial z}=A_0+A_1\cos\omega t, \qquad t>0$$

where

A_0 → constant amplitude of the pressure gradient,
A_1 → amplitude of the pulsatile component giving rise to systolic and diastolic pressure and
$\omega=2\pi f_p$, where f_p is the pulse frequency.

2.2. Boundary Conditions

It is assumed that no flow takes places when the system is at rest.

$$u_r=0, \quad v_r=0, \quad u_z=0, \quad v_z=0.$$

There is no radial flow along the axis of the alveolar sac and the axial velocity gradient of the streaming air may be implicit to be equal to zero.

$$u_r=0, \quad \frac{\partial u_z}{\partial r}=0, \quad v_r=0, \quad \frac{\partial v_z}{\partial r}=0.$$

At the surface of the wall,

$$u_r=0, \quad v_r=0, \quad u_z=0, \quad v_z=0,$$

i.e., the no-slip boundary condition is imposed.

3. Methodology

3.1. Transformation of the Governing Equations

On introducing the following non-dimensional quantities

$$u_x = \frac{u_r}{u_0}, \quad u_y = \frac{u_z}{u_0}, \quad v_x = \frac{v_r}{u_0}, \quad v_y = \frac{v_z}{u_0}, \quad x = \frac{r}{R}, \quad y = \frac{z}{R},$$
$$p = \frac{p'}{\rho u_0^2}, \quad \tau = \frac{tu_0}{R}, \quad \mathrm{Re} = \frac{Ru_0}{\nu}, \quad B = \frac{KRN_0}{\rho}, \quad \gamma = \frac{mu_0}{KR}.$$

Equations (1-4) together with boundary conditions obtain the following form:

$$\frac{\partial u_x}{\partial x} + \frac{u_x}{x} + \frac{\partial u_y}{\partial y} = 0, \tag{7}$$

$$\frac{\partial u_y}{\partial \tau} + u_x \frac{\partial u_y}{\partial x} + u_y \frac{\partial u_y}{\partial y} = -\frac{\partial p}{\partial y} + \frac{1}{\mathrm{Re}}\left(\frac{\partial^2 u_y}{\partial x^2} + \frac{1}{x}\frac{\partial u_y}{\partial x} + \frac{\partial^2 u_y}{\partial y^2}\right) + B(v_y - u_y), \tag{8}$$

$$\frac{\partial v_x}{\partial x} + \frac{v_x}{x} + \frac{\partial v_y}{\partial y} = 0, \tag{9}$$

$$\frac{\partial v_y}{\partial \tau} + v_x \frac{\partial v_y}{\partial x} + v_y \frac{\partial v_y}{\partial y} = \frac{u_y - v_y}{\gamma}. \tag{10}$$

3.2. Transformation of the boundary conditions

$$u_x = 0, \quad v_x = 0, \quad u_y = 0, \quad v_y = 0. \qquad \text{at} \quad \tau = 0,$$
$$u_x = 0, \quad \frac{\partial u_y}{\partial x} = 0, \quad v_x = 0, \quad \frac{\partial v_y}{\partial x} = 0. \qquad \text{at} \quad x = 0,$$
$$u_x = 0, \quad v_x = 0, \quad u_y = 0, \quad v_y = 0. \qquad \text{at} \quad x = 1.$$

The finite difference scheme is used to solve the governing transformed equation by using central difference approximations for all the spatial derivatives (Smith 1985). The iterative method has been found to be quite effective in solving the equation numerically for different time periods. Three special meshes, i.e., coarse, fine and very fine, were engaged to check grid independence of the results. At last, the fine mesh was preferred for the current work since it produced the similar results as the very fine mesh and is computationally more efficient. The convergence of the calculated solution was evaluated by taking into account the stabilized residuals of each flow variable. Convergence was attained when the stabilized residuals were < 10^{-3}. The mesh dependency of the solution was also inspected by working out the flow field in a finer mesh. There was no major difference in the calculations between the coarse and the fine mesh. The time step was chosen to be $\Delta t = 0.001$, $\Delta y = 0.05$ and $\Delta x = 0.05$ are the grid spacing. These results are subsequently used to solve equations numerically.

To use finite difference scheme (7), (8) and (9) (at $x = 0$), converts as

$$\lim_{x \to 0} \frac{u_x}{x} = \lim_{x \to 0} \frac{\partial u_x}{\partial x},$$
$$\lim_{x \to 0} \frac{1}{x}\frac{\partial u_y}{\partial x} = \lim_{x \to 0} \frac{\partial^2 u_y}{\partial x^2},$$

$$\lim_{x\to 0}\frac{v_x}{x}=\lim_{x\to 0}\frac{\partial v_x}{\partial x}.$$

4. Discretization of the components

The discretization of axial velocity $u_z(x,y,t)$ is written as $u_z(x_i,y_j,t_k)$ or $(u_z)^k_{i,j}$. We define

$$\begin{aligned}
&x_i = i.\Delta x; && i=0,1,2,\ldots,N, \quad \text{where} \quad x_N=1.0.\\
&y_i = j.\Delta y; && j=0,1,2,\ldots,M.\\
&t_k=(k-1)\Delta t; && k=1,2,\cdots.
\end{aligned}$$

Using the discretization techniques the axial velocity from (8) (at x = 0), has its discretized form as:

$$\begin{aligned}
(u_y)^{k+1}_{i,j} &= (u_y)^k_{i,j}\left[1-\frac{4.\Delta\tau}{\Delta x^2}.\frac{1}{\text{Re}}-\frac{2.\Delta\tau}{\Delta y^2}.\frac{1}{\text{Re}}-B.\Delta\tau\right]-\frac{\Delta\tau}{2.\Delta x}\left[(u_x)^k_{i,j}.(u_y)^k_{i+1,j}+(u_x)^k_{i,j}.(u_y)^k_{i-1,j}\right]\\
&-\frac{\Delta\tau}{2.\Delta y}\left[(u_y)^k_{i,j}.(u_y)^k_{i,j+1}+(u_y)^k_{i,j}.(u_y)^k_{i,j-1}\right]+\frac{2.\Delta\tau}{\text{Re}.(\Delta x)^2}\left[(u_y)^k_{i+1,j}+(u_y)^k_{i-1,j}\right]\\
&+\frac{\Delta\tau}{\text{Re}.(\Delta y)^2}\left[(u_y)^k_{i,j+1}+(u_y)^k_{i,j-1}\right]+B.\Delta\tau.(v_y)^k_{i,j}+\left(A_0+A_1\cos(\omega\tau R/u_0)\right)\Delta\tau,
\end{aligned}$$

at $0 < x \le 1$, (8) becomes

$$\begin{aligned}
(u_y)^{k+1}_{i,j} &= (u_y)^k_{i,j}\left[1-\frac{2.\Delta\tau}{(\Delta x)^2}.\frac{1}{\text{Re}}-\frac{2.\Delta\tau}{(\Delta y)^2}.\frac{1}{\text{Re}}-B.\Delta\tau\right]-\frac{\Delta\tau}{2.\Delta x}\left[(u_x)^k_{i,j}.(u_y)^k_{i+1,j}+(u_x)^k_{i,j}.(u_y)^k_{i-1,j}\right]\\
&-\frac{\Delta\tau}{2.\Delta y}\left[(u_y)^k_{i,j}.(u_y)^k_{i,j+1}+(u_y)^k_{i,j}.(u_y)^k_{i,j-1}\right]+\frac{\Delta\tau}{\text{Re}.(\Delta y)^2}\left[(u_y)^k_{i,j+1}+(u_y)^k_{i,j-1}\right]\\
&+(u_y)^k_{i+1,j}\left[\frac{\Delta\tau}{\text{Re}.x.2.\Delta x}+\frac{\Delta\tau}{\text{Re}.(\Delta x)^2}\right]+(u_y)^k_{i-1,j}\left[\frac{\Delta\tau}{\text{Re}.(\Delta x)^2}-\frac{\Delta\tau}{\text{Re}.x.2.\Delta x}\right]\\
&+B.\Delta\tau.(v_y)^k_{i,j}+\left(A_0+A_1\cos(\omega\tau R/u_0)\right)\Delta\tau.
\end{aligned}$$

After discretization, the radial velocity can be calculated from (7) (at x = 0)

$$(u_x)^{k+1}_{i+1,j} = (u_x)^{k+1}_{i,j}-\frac{\Delta x}{2.\Delta y}\left[(u_y)^{k+1}_{i,j+1}-(u_y)^{k+1}_{i,j}\right],$$

at $0 < x \le 1$, (7) becomes

$$(u_x)^{k+1}_{i+1,j}=\left(1-\frac{\Delta x}{x}\right)(u_x)^{k+1}_{i,j}-\frac{\Delta x}{\Delta y}\left[(u_y)^{k+1}_{i,j+1}-(u_y)^{k+1}_{i,j}\right].$$

The axial velocity of dust particles can be observed from (10) and its discretized form is

$$\left(v_y\right)_{i,j}^{k+1} = \left(1-\frac{\Delta\tau}{\gamma}\right)\left(v_y\right)_{i,j}^{k} + \frac{\Delta\tau}{\gamma}\left(u_y\right)_{i,j}^{k} - \frac{\Delta\tau}{2.\Delta x}\left(v_x\right)_{i,j}^{k}\left[\left(v_y\right)_{i+1,j}^{k} - \left(v_y\right)_{i-1,j}^{k}\right]$$
$$-\frac{\Delta\tau}{2.\Delta y}\left(v_y\right)_{i,j}^{k}\left[\left(v_y\right)_{i,j+1}^{k} - \left(v_y\right)_{i,j-1}^{k}\right].$$

The radial velocity of dust particles can be calculated from (9) (at x = 0), with its discretized form as

$$\left(v_x\right)_{i+1,j}^{k+1} = \left(v_x\right)_{i,j}^{k+1} - \frac{\Delta x}{2.\Delta y}.\left[\left(v_y\right)_{i,j+1}^{k+1} - \left(v_y\right)_{i,j}^{k+1}\right],$$

at $0 < x \leq 1$, (9) becomes

$$\left(v_x\right)_{i+1,j}^{k+1} = \left(1-\frac{\Delta x}{x}\right).\left(v_x\right)_{i,j}^{k+1} - \frac{\Delta x}{\Delta y}.\left[\left(v_y\right)_{i,j+1}^{k+1} - \left(v_y\right)_{i,j}^{k+1}\right].$$

The initial and boundary conditions in discretized form are as follows:

$$\left(u_x\right)_{1,j}^{k} = 0, \quad \left(u_y\right)_{0,j}^{k} = \left(u_y\right)_{2,j}^{k}, \quad \left(v_x\right)_{1,j}^{k} = 0, \quad \left(v_y\right)_{0,j}^{k} = \left(v_y\right)_{2,j}^{k},$$

$$\left(u_x\right)_{N+1,j}^{k} = 0, \quad \left(u_y\right)_{N+1,j}^{k} = 0, \quad \left(v_x\right)_{N+1,j}^{k} = 0, \quad \left(v_y\right)_{N+1,j}^{k} = 0,$$

$$\left(u_x\right)_{i,j}^{1} = 0, \quad \left(u_y\right)_{i,j}^{1} = 0, \quad \left(v_x\right)_{i,j}^{1} = 0, \quad \left(v_y\right)_{i,j}^{1} = 0.$$

Now, we solve the problem using above discretization techniques for fluid and dust particle velocities.

5. Results and Discussions

Numerical computations have been carried out using the following parameter values (Ismail et al. 2007, Kapur 1985, Mandal 2005).

$$R = 125\mu\text{m}, \quad N_0 = 0.02504\times 10^{6}/\text{cm}^3, \quad u_0 = 0.3\text{cm/s}, \quad r_p = 50\text{nm}, \quad m = 0.0002\text{gm},$$
$$\rho = 1.185\times 10^{-3}\text{g/cm}^3, \quad f_p = 1.2\,\text{Hz}, \quad A_0 = 10\text{gm/cm}^2\text{s}^2, \quad A_1 = 0.2A_0.$$

The parabolic velocity profile that was forced at the inlet of the central part was preserved for most of the central lumen of the first generation. Only a partial segment of the flow goes through the alveolar cavities and recirculated gradually within them.

Figure 3 shows the deposition pattern in the complete configuration (Darquenne 2001). The central part with the eight peripheral parts is exposed. Particles that were deposited throughout the inspiration phase are characterized by gray circles, and those deposited throughout the expiration phase are characterized by black circles. Particles that stay behind in suspension at the end of expiration are also exposed (white circles). The dark gray circles exteriors the configuration stand for the particles that have runaway the configuration throughout expiration. The deposition pattern exposed in Figure 2 is obviously heterogeneous. The major cause of deposition of 100nm-diameter particles is gravitational sedimentation that reasons particles to resolve in the alveolar cavities, at the base of every configuration.

The flow outlines explain similar shapes at different time levels as illustrated in Figure 4. The steady-state velocity profile of fluid approximately equivalent the instantaneous axial velocity when t = 0.7s at $Re_{\text{in}} = 1201$ (Figure 4).

A comparison of axial velocity of particles along horizontal symmetric axis at the alveolar ducts in the transient state at $t = 0.2$s and $t = 0.7$s and for steady state with a Reynolds-number-equivalent profile are shown in Figure 5.

All velocity distributions display extremely nonlinear profile shapes. At $t = 0.7$s, the flow velocity has the biggest value. Once more, the flow patterns illustrate a bit similar shapes at different time levels. The radial velocities of fluid along the horizontal symmetric axis at the alveolar ducts under different conditions have presented in Figure 6. For the transient case, velocity profiles are extensively different at $t = 0.2$s and $t = 0.7$s caused by the transient effect (Zhang and Kleinstreuer 2002). The steady-state velocity profile of fluid is approximately equivalent to the instantaneous radial velocity when t = 0.7s at $Re_{\text{in}} = 1201$.

A comparison of radial velocity of particles along horizontal symmetric axis at the alveolar ducts in the transient state at $t = 0.2$s and $t = 0.7$s and for steady state with a Reynolds-number-equivalent profile is described in Fig. 7. In this figure, velocity profiles of particles are also extensively different at $t = 0.2$s and $t = 0.7$s caused by the transient effect whereas the steady-state velocity profile of particles is approximately equivalent to the instantaneous radial velocity when t = 0.7s.

Table 1 records the average and maximum velocity at the alveolar ducts for different t ($Re_{\text{in}} = 1201$). This demonstrates that maximum values are at $t = 0.7$s rather than at $t = 0.2$s.

We also conclude that both the fluid and dust particles possess a maximum velocity on the axis of the tube and fluid particles move faster than the dust particles.

6. Conclusion

The model presents a device to improve and identify the locations of deposition of particles in the alveolar ducts of the human lung. The numerical data explained in this study also maintain this inspection as deposited particles were situated inside the alveolar cavities (Figure 3).

The representation was used to suggest the transport of 100nm-diameter particles for one orientation of the configuration, whereas imitations with different particle sizes and for different orientations of the configuration regarding the gravity vector are required to depict a more common termination. An improved understanding of the outcome of aerosols in the alveolar zone of the lung as granted by these models may also be valuable in purposes for example inhalation drug therapy.

An important observation is that a huge number of particles are unsuccessful to way out the configuration at the end of expiration and that most of these particles stay behind in suspension in the distal part of the configuration. According to this throughout the consequent breath, these particles will go deeper in the lung and ultimately deposit. Inhaled particles may consequently attain distal areas of the lung. This examination may have significant suggestions in occupational sanitation and specifically the effect of inhalation of the airborne pollutants to human health.

Acknowledgement:

Financial support by grant in aid to one of the authors (Anju Saini), from National Board for Higher Mathematics (NBHM), Government of India is gratefully acknowledged.

REFERENCES

Cheng, K.H., Cheng, Y.S., Yeh, H.C., Guilmette, R.A., Simpson S.Q. and Yang, Y.H. (1996). In vivo: measurements of nasal airway dimensions and ultrafine aerosol deposition in the human nasal and oral airways, J. Aerosol Sci. 27, 785-801.

Cheng, K.H. and Swift, D.L. (1995). Calculation of total deposition fraction of ultrafine aerosols in human extra thoracic and intrathoracic regions, Aerosol Sci. and Tech. 22, 194-201.

Cohen, B.S., Sussman R.G. and Lippmann, M. (1990). Ultrafine particle deposition in a human tracheo-bronchial cast, Aerosol Sci. and Tech. 12, 1082-1091.

Darquenne, C. (2001). A realistic two-dimensional model of aerosol transport and deposition in the alveolar zone of the human lung, J. Aerosol Sci. 32, 1161-1174.

Hofmann, W., Golser, R. and Balashazy, I. (2003). Inspiratory deposition efficiency of ultrafine particles in a human airway bifurcation model, Aerosol Sci. and Tech. 37, 988-994.

Ingham, D.B. (1991). Diffusion of aerosols in the entrance region of a smooth cylindrical pipe, J. Aerosol Sci. 22(3), 253-257.

Ismail, Z., Abdullah, I., Mustapha, N. and Amin, N. (2007). A power-law model of blood flow through a tapered overlapping stenosed artery, Appl. Math. Comput. 195(2), 669-680.

Kapur, J.N. (1985). *Mathematical Models in Biology and Medicine,* East-West Press, Pvt. Ltd., New Delhi.

Kelly, J.T., Asgharian, B., Kimbell, J.S. and Wong, B.A. (2004). Particle deposition in human nasal airway replicas manufactured by different methods. Part II: Ultrafine particles, Aerosol Sci. and Tech. 38, 1072-1079.

Kim, C.S. and Jaques, P.A. (2004). Analysis of total respiratory deposition of inhaled ultrafine particles in adult subjects as various breathing patterns, Aerosol Sci. and Tech. 38, 525-540.

Kim, C.S. and Jaques, P.A. (2000). Respiratory dose of inhaled ultrafine particles in healthy adults. Philosophical Transactions of the Royal Society of London Series A—Math, Phys. and Eng. Sci. 358, 2693-2705.

Kleinstreuer, C. (2003). *Two-phase Flow: Theory and Applications,* Taylor & Francis, New York.

Lee, D. and Lee, J. (2002). Dispersion of aerosol bolus during one respiration cycle in a model lung airway, J. Aerosol Sci. 33(9), 1219-1234.

Mandal, P.K. (2005). An unsteady analysis of non-Newtonian blood flow through tapered arteries with a stenosis, Int. J. Non-Linear Mech. 40, 151-164.

Martonen, T., Zhang, Z. and Yang, Y. (1996). Particle diffusion with entrance effects in a smooth-walled cylinder, J. Aerosol Sci. 27(1), 139-150.

Moskal, A., Gradon, L. (2002). Temporary and spatial deposition of aerosol particles in the upper human airways during breathing cycle, J. Aerosol Sci. 33(11), 1525-1539.

Nayfeh, A.H. (1966). Oscillating two phase flow through a rigid pipe, AIAA. 4(10), 1868-1870.

Saini, A., Katiyar, V.K. and Parida, M. (2016). Two dimensional model of pulsatile flow of a dusty fluid through a tube with axisymmetric constriction, World Journal of Modelling and Simulation, 12(1), 70-78.

Saini, A., Katiyar, V.K. and Pratibha (2014). Effects of First Order Chemical Reactions on the Dispersion Coefficient Associated With Laminar Flow through the Lungs, Int. J. Biomath. **7**(2), 1450021, 1-12.

Saini, A., Katiyar, V.K. and Pratibha (2015). Numerical simulation of gas flow through a biofilter in lung tissues, World Journal of Modelling and Simulation, 11(1), 33-42.

Severinghaus, J.W., Astrup, P. and Murray, J.F. (1998). Blood gas basics & the respiratory system, Am. J. Respir. Crit. Care Med. 157(4), S114-S122.

Shi, H., Kleinstreuer, C., Zhang, Z. and Kim, C.S. (2004). Nanoparticle transport and deposition in bifurcating tubes with different inlet conditions, Phys. Fluids. 16, 2199-2213.

Smith, G.D. (1985). *Numerical solution of partial differential equations*, Third ed. Oxford Univ. Press.

Smith, S., Cheng, U.S. and Yeh, H.C. (2001). Deposition of ultrafine particles in human tracheobronchial airways of adults and children, Aerosol Sci. Tech. 35, 697-709.

Sturm, R. (2015). A computer model for the simulation of nanoparticle deposition in the alveolar structure of the human lungs, Ann. Transl. Med. 3(19), 281.

Xi, J.X. and Longest, P.W. (2008a). Effects of oral airway geometry characteristics on the diffusional deposition of inhaled nanoparticles, J. Biomech. Eng. Trans. ASME. 130(1), 0110081, 1-16.

Zhang, Z., Kleinstreuer, C., Donohue, J.F. and Kim, C.S. (2005). Comparison of micro- and nano-size particle depositions in a human upper airway model, J. Aerosol Sci. 36, 211-233.

Zhang, Z. and Kleinstreuer, C. (2004). Airflow structures and nano-particle deposition in a human upper airway model, J. Compute. Phys. 198, 178-210.

Zhang, Z. and Kleinstreuer, C. (2002). Transient airflow structures and particle transport in a sequentially branching lung airway model. Phys. Fluids. 14(2), 862.

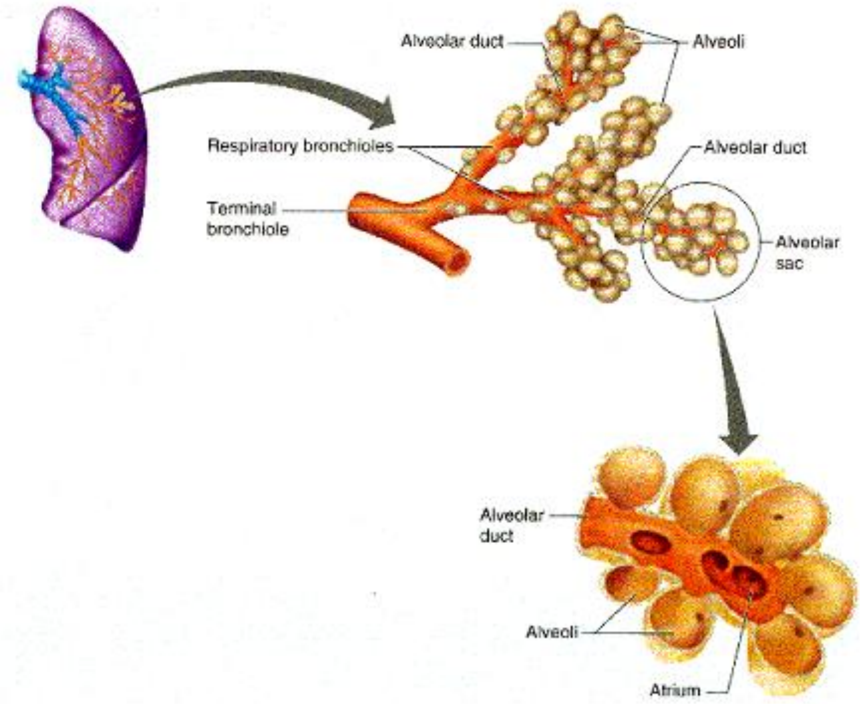

Figure 1. Respiratory zones (Shi et al. 2004)

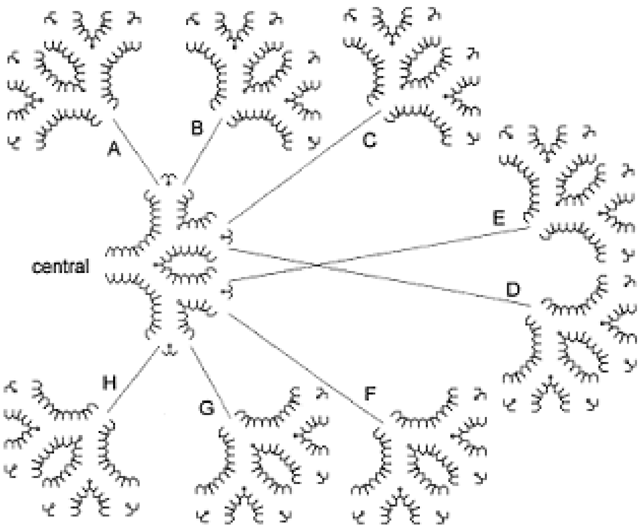

Figure 2. Illustration of the complete configuration. At every one of the eight outlets of the central part, an alike configuration was linked (peripheral units A-H) to attain a 6-generation configuration of alveolated ducts (Darquenne 2001)

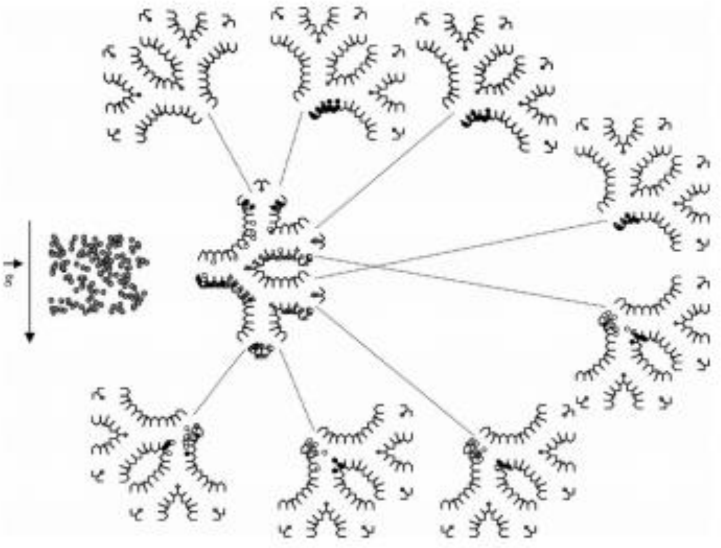

Figure 3. Deposition pattern in the complete configuration. All particles that go into the configuration throughout inspiration are accounted for in the figure (Darquenne 2001)

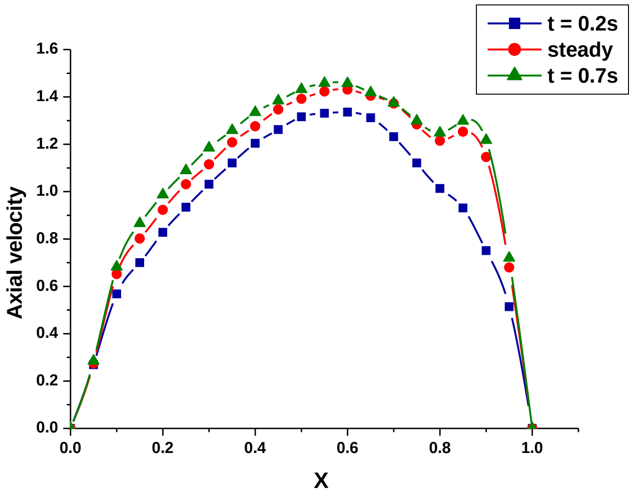

Figure 4. Comparison of Axial velocity profiles of fluid along horizontal symmetric axis

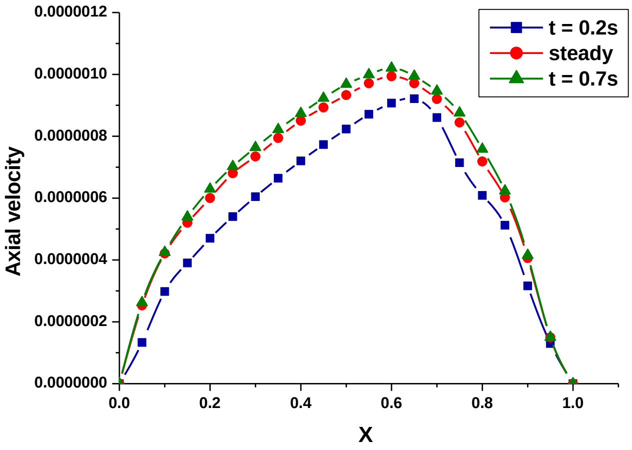

Figure 5. Comparison of Axial velocity profiles of particles along horizontal symmetric axis

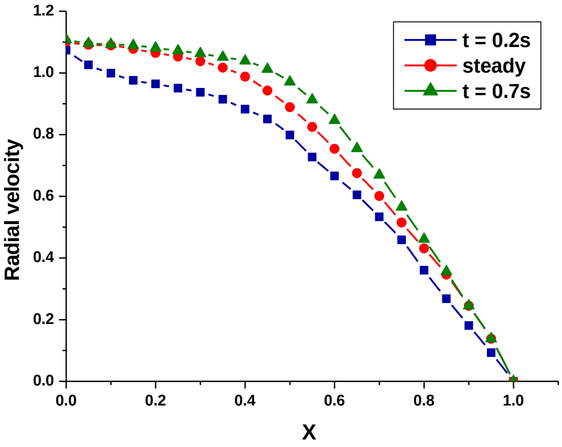

Figure 6. Comparison of Radial velocity profiles of fluid along horizontal symmetric axis

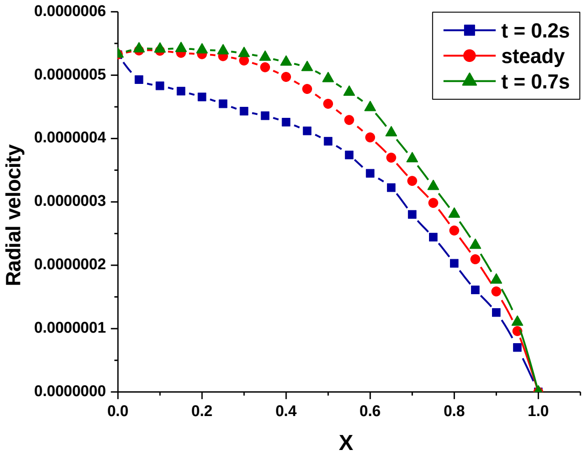

Figure 7. Comparison of Radial velocity profiles of particles along horizontal symmetric axis

Table 1. Average and maximum velocity at different *t* (*Re*$_{\text{in}}$ = 1201)

			t = 0.2 s	Steady	t = 0.7 s
Fluid	Average value	Radial velocity	0.679	0.756	0.792
		Axial velocity	0.894	1.011	1.047
	Maximum value	Radial velocity	1.074	1.101	1.108
		Axial velocity	1.336	1.431	1.458
Particles	Average value	Radial velocity	3.40×10^{-7}	3.92×10^{-7}	4.12×10^{-7}
		Axial velocity	5.36×10^{-7}	6.31×10^{-7}	6.52×10^{-7}
	Maximum value	Radial velocity	5.32×10^{-7}	5.39×10^{-7}	5.42×10^{-7}
		Axial velocity	9.21×10^{-7}	9.94×10^{-7}	1.02×10^{-6}